

A Submersible Position Prediction and Search-and-Rescue Path Planning Model Based on the Bidirectional Long Short-Term Memory Network

Qiaoru Li

Software College
Northeastern University
Shenyang, China
emberlqr@gmail.com

Yueyang Zhang

College of Science
Northeastern University
Shenyang, China
20221938@stu.neu.edu.cn

Yekai Li

College of Information Science and Engineering
Northeastern University
Shenyang, China
20221923@stu.neu.edu.cn

Li Zhang*

Software College
Northeastern University
Shenyang, China

* Corresponding author: zhangl@swc.neu.edu.cn

Abstract—The navigation safety of submersibles is becoming an important issue in this field. In response to submersibles encountering emergencies, we innovatively propose a position prediction model based on the excellent adaptability of the Bidirectional Long Short-Term Memory (BiLSTM) Network to time series, combined with the six-degree-of-freedom motion model of the submersible. This model can predict the position distribution of the submersible within a certain period after losing propulsion power with relative accuracy, as shown in our simulation result of the Ionian Sea. As an application of this technology, we further leverage this position prediction model to introduce a search and rescue path planning model using Monte Carlo Simulation and Genetic Algorithm (GA), providing potential path planning schemes for rescue vessels. This study offers a new perspective and methodology for applying neural network technology to position prediction, serving as a reference for future research.

Keywords—position prediction; BiLSTM Network; six-degree-of-freedom motion model; Monte Carlo Simulation; Genetic Algorithm

I. INTRODUCTION

The advancement of submersible technology plays a crucial role in humanity's exploration of the oceans, offering vast opportunities for scientific research, resource discovery, and environmental monitoring. However, the unpredictable marine environment, characterized primarily by changing currents and complex hydrodynamic forces, poses significant challenges to the navigational safety of submersibles. The tragic incident of the "Titan" submersible in June 2023 shocked the world, underscoring the potential dangers of deep-sea exploration under extreme oceanic conditions and emphasizing the urgency of predicting submersible positions and search-and-rescue operations.

Due to the variations in size and direction of ocean currents with time and location, accurately modeling the motion of

submersibles with current interference is challenging. The real marine environment features extremely complex currents influenced by various environmental factors, and the absence of a publicly available ocean current database complicates this further. In his research on the mathematical model of underwater vehicle motion, Li Dejun considered six degrees of freedom movement. By transforming between the inertial coordinate system and the submersible's coordinate system, the spatial kinematic model of the submersible was derived [1]. Gabl and others studied the effects of ocean currents and waves on the hydrodynamics of the Blue ROV2 in the FloWave pool, providing both raw experimental data and processed datasets as references for experimental validation, testing, and development of ROV position control algorithms [2]. Xu Xiang combined fuzzy logic systems with feedback linearization methods to design a three-dimensional trajectory tracking control law for underactuated AUVs [3]. Mansour and colleagues presented multi-objective path planning in underwater environments with multiple static obstacles, solved by an improved genetic algorithm [4].

Upon reviewing these studies, it is observed that existing position prediction schemes primarily employ kinematic principles for relatively direct computation, focusing on mathematical calculations and solutions without the capacity to integrate the submersible's motion behavior from other time periods to predict future motion behavior. Considering this, our research aims to overcome this limitation by introducing a time-series-based deep learning method, namely the Bidirectional Long Short-Term Memory (BiLSTM) network. The BiLSTM network is capable of effectively processing and analyzing time-series data, capturing the long-term dependencies in the submersible's motion behavior, thereby offering a more accurate prediction of future positions. Compared to traditional kinematic models, this method not only considers the current dynamic state but also integrates potential patterns and trends from historical

data, providing a novel perspective for submersible position prediction and search-and-rescue path planning.

Our contributions are summarized in two aspects:

- We develop a position prediction model based on the six-degree-of-freedom motion model and the BiLSTM network, capable of predicting the future position of a submersible over a certain period after it loses propulsion power. This is achieved by learning from motion data and ocean current environmental data transmitted during normal communication periods between the submersible and its mother ship.
- As an application of the position prediction model, we also construct a search and rescue path planning model using Monte Carlo Simulation and Genetic Algorithm, based on this model. This model is capable of providing recommended search and rescue path schemes starting from a selected position.

II. POSITION PREDICTION MODEL

A. Derivation of Six-degree-of-freedom Motion Model

In the study of the six-degree-of-freedom motion of deep-sea submersibles, a commonly used coordinate system approach involves two coordinate systems: the inertial coordinate system, fixed to the Earth (Earth coordinate system), and the body-fixed coordinate system, attached to the submersible (submersible coordinate system), both utilizing the right-hand rule. Expressions for ocean current velocity in both coordinate systems are presented as Equation 1 and 2, assuming ocean current velocity in the inertial coordinate system as v_m , with horizontal and vertical flow direction angles denoted as φ_m and θ_m , respectively.

$$\begin{aligned} v_m &= (v_{mx}, v_{my}, v_{mz})^T \\ &= (v_m \cos \varphi_m \cos \theta_m, v_m \sin \varphi_m \cos \theta_m, -v_m \sin \theta_m)^T \end{aligned} \quad (1)$$

$$\begin{aligned} V_{ms} &= (v_{mx}, v_{my}, v_{mz})^T \\ &= T^{-1} (v_m \cos \varphi_m \cos \theta_m, v_m \sin \varphi_m \cos \theta_m, -v_m \sin \theta_m)^T \end{aligned} \quad (2)$$

Here V_{ms} represents the current velocity in the submersible coordinate system, and T signifies the rotational transformation matrix from the submersible coordinate system to the inertial coordinate system (T is an orthogonal matrix). Consequently, the expressions for the components of the ocean current velocity in the submersible coordinate system can be derived, as indicated in Equation 3, 4 and 5.

$$v_{mx} = v_m \cos(\varphi_m - \varphi) \cos \theta_m \cos \theta + v_m \sin \theta_m \sin \theta \quad (3)$$

$$\begin{aligned} v_{my} &= v_m \cos(\varphi_m - \varphi) \cos \theta_m \sin \theta \sin \phi + \\ &\quad v_m \sin(\varphi_m - \varphi) \cos \theta_m \cos \phi - v_m \sin \theta_m \cos \theta \sin \phi \end{aligned} \quad (4)$$

$$\begin{aligned} v_{mz} &= v_m \cos(\varphi_m - \varphi) \cos \theta_m \sin \theta \cos \phi - \\ &\quad v_m \sin(\varphi_m - \varphi) \cos \theta_m \sin \phi - v_m \sin \theta_m \cos \theta \cos \phi \end{aligned} \quad (5)$$

The relative velocity of the submersible to the ocean current in the submersible coordinate system is represented as $v_a = v - v_m$. By substituting the original velocity v with the relative velocity

v_a of the submersible to the ocean current in the submersible coordinate system, and incorporating it into the six-degree-of-freedom spatial equation set of the submersible, the unpowered motion model of the submersible under the influence of ocean currents can be obtained, as depicted in Equation 6 after appropriate simplification. [5][6]

$$\begin{aligned} m[v_a - w_a p + u_a r] &= \frac{1}{2} \rho L^2 [Y'_0 u_a^2 + Y'_v u_a v_a + Y'_{vw} v_a w_a] + \\ &\quad \frac{1}{2} \rho L^3 Y'_{v|r} \frac{v_a}{|v_a|} \left| (v_a^2 + w_a^2)^{\frac{1}{2}} \right| |r| + \frac{1}{2} \rho L^2 Y'_{v|v} v_a \left| (v_a^2 + w_a^2)^{\frac{1}{2}} \right| \end{aligned} \quad (6)$$

In this research, we use $M = \frac{1}{2} \rho v_c^2 C_d l h^2$ to simulate the moment on the submersible M , where C_d is the coefficient of drag, and l and h respectively represent the length and height of the submersible. Part of the vectors in Equation 6 use the convention symbols in the six-degree-of-freedom model, as shown in Table 1.

Table 1. Some Vectors and their Symbols

Vector	Meaning	x-axis	y-axis	z-axis
V_s	Velocity of submersible	u	v	w
Ω	Angular velocity of submersible	p	q	r
F	The force on submersible	X	Y	Z
M	The moment of submersible	K	M	N

B. BiLSTM Network Design

In the realm of dynamic prediction for submersibles, the BiLSTM network stands out for its exceptional handling of time series data. Unlike traditional unidirectional LSTM networks, the BiLSTM network is capable of considering both past and future information, thereby offering a more comprehensive contextual understanding when dealing with data that depends on temporal sequences. This feature allows the BiLSTM network to more accurately capture dynamic changes when predicting the instantaneous velocity and position of submersibles in complex marine environments. By leveraging the bidirectional long short-term memory network, our model can effectively learn from and infer the motion trends of submersibles based on historical data, significantly enhancing the accuracy and reliability of predictions.

As shown in Figure 1, the BiLSTM network we constructed receives an input vector $X=[v_1, v_2, \dots, v_n, v_p]$ at each prediction instance, where (v_1, v_2, \dots, v_n) represent the sequence of true velocity values of the submersible during the time interval Δt prior to the current moment, and v_p represents the instantaneous velocity prediction value calculated through the six-degree-of-freedom motion model. The BiLSTM network aligns these velocity inputs in chronological order and analyzes the velocity sequences before and after a given moment through two LSTM networks respectively. Data learning and filtering are collaboratively conducted through the input gate, output gate, and forget gate, facilitating the comprehensive analysis and prediction of the submersible's velocity.

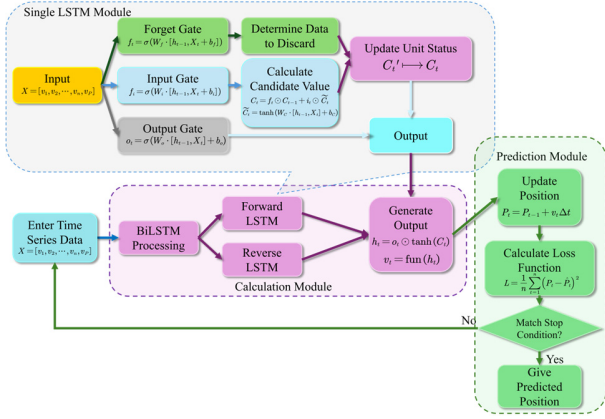


Figure 1. Our BiLSTM Network

In Figure 1, f_t , i_t , o_t respectively represent the activation values of the forget gate, input gate, and output gate. C_t represents the candidate value of the LSTM unit, which is the cell state, h_t is the output, σ is the sigmoid function, and W and b are the weight and bias parameters, respectively. \odot represents element-wise multiplication. Function $\text{fun}(h_t)$ represents the transformation layer from h_t to v_t . We employ the Mean Square Error (MSE) as the loss function.

C. Model Training

We choose part of the Ionian Sea, a subregion of the Mediterranean, as our target simulation area. We obtain the ocean current data and seafloor topography data from [7][8][9]. The geographic region under investigation spans a rectangular area characterized by longitudinal coordinates ranging from 16.02°E to 20.60°E and latitudinal coordinates ranging from 35.65°N to 37.66°N. To facilitate our analysis, we employ a gridding process to transform the downloaded Esri ASCII depth data into a structured 100×100 grid. This results in the division of the water depth dataset into a total of 10,000 small grid cells, and subsequently, we apply a rigorous fifth-order spline interpolation technique to yield a 100×100 matrix representing the water depth distribution. Subsequently, we utilize this interpolated matrix to generate a Digital Elevation Model (DEM), as shown in Figure 2. A simulation of currents in some of the seawater depth planes is shown in Figure 3.

For ocean current distribution data, we employ K-means clustering to categorize accessible depths within 2000 kilometers of the research area's origin into four layers. From each layer, we select and extract 10 exemplary ocean current scenarios for subsequent analytical investigations.

Based on PyTorch, we divide the dataset based on a 100×100 grid into 10,000 parts, splitting them in a 7:3 ratio for the training and testing sets, respectively. In considering ocean currents as the primary factor influencing the movement of lost submersibles, we conduct K-means clustering analysis on the variations in ocean currents. Hence, the Unit-Length Temporal

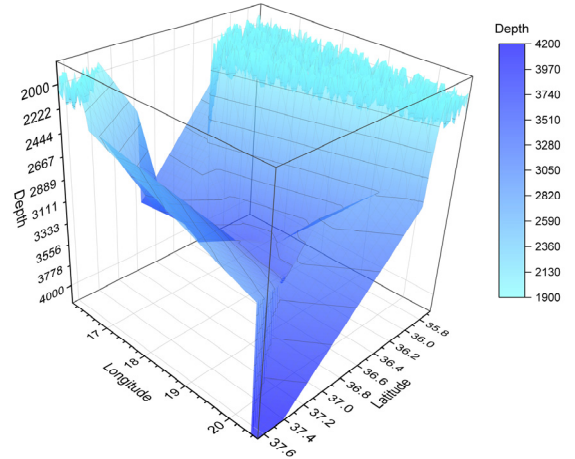


Figure 2. The DEM of the Studied Area

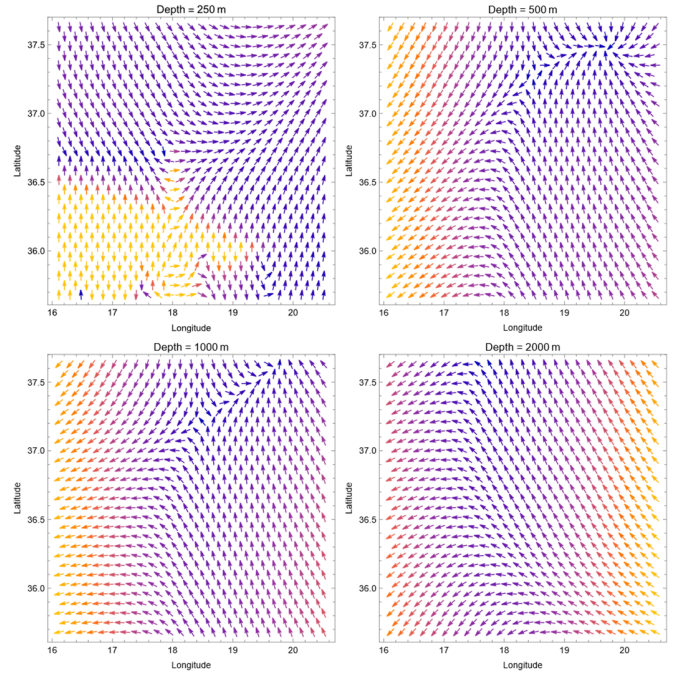


Figure 3. The Instantaneous Ocean Currents Simulation in Different Depths in the Studied Area

Sequence (UTS) for the four BiLSTM network models are set to 0.846s, 1.912s, 2.273s, and 3.158s, respectively. The

accuracy curves of these four models on the training set are illustrated in Figure 4.

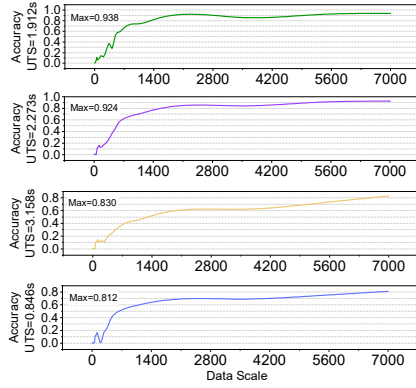


Figure 4. Accuracy Curve of Predictions on the Training Set

D. Model Testing and Data Analysis

We designate every 70 data points in the training set as one training epoch with a sum of 100. The variation of the predictive accuracy of the model on the test set, consisting of 3000 data points, across different training cycles is depicted in Figure 5. In this context, we posit that a predictive calculation discrepancy within 5% of the current ocean current velocity for each dimension is considered indicative of accurate forecasting. Based on the training and prediction results, we depict the predicted trajectories and simulated real trajectories for two UTSs that exhibit relatively excellent performance, as shown in Figure 6 and 7.

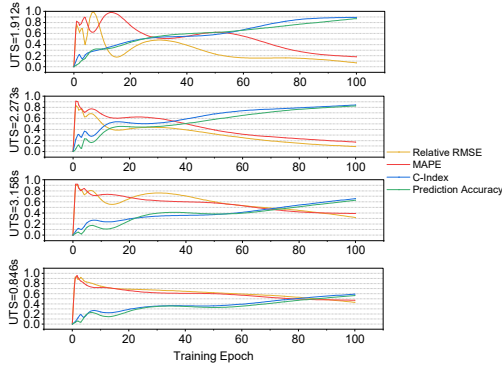


Figure 5. Prediction Outcomes on the Test Set across Various Training Epochs

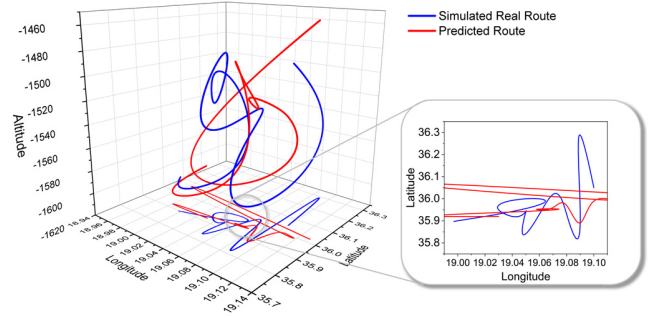


Figure 6. Route Prediction Result with UTS=1.912s

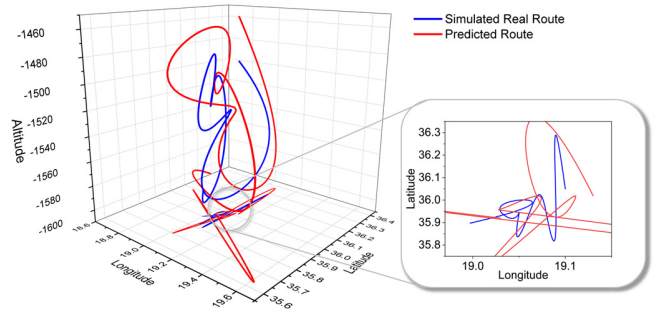


Figure 7. Route Prediction Result with UTS=2.273s

Based on the results shown in Figure 5, 8, and 9, it is observed that the two BiLSTM models with UTS=1.912s and UTS=2.273s exhibit significantly superior performance in terms of training set accuracy curves and test set outcomes compared to the models with UTS=3.158s and UTS=0.846s. Examining the position prediction curves reveals that the model with UTS=1.912s demonstrates slightly stronger predictive capabilities than the model with UTS=2.273s, achieving accurate shape predictions for partial trajectories and displaying lower positional errors.

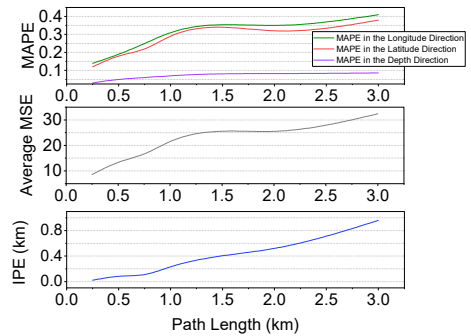


Figure 8. Some Evaluation Metrics Varying with Prediction Distance with UTS=1.912s

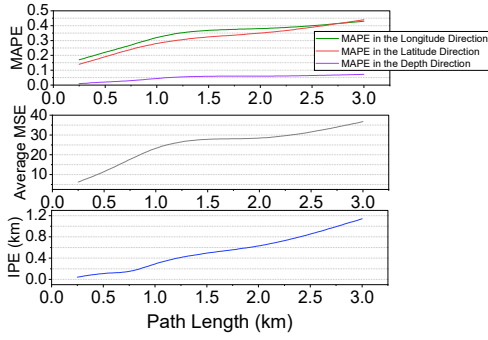


Figure 9. Some Evaluation Metrics Varying with Prediction Distance with UTS=2.273s

Through the analysis of the data, in the context of long-distance position prediction, the model with UTS=2.273s outperforms the model with UTS=1.912 in terms of prediction accuracy, MSPE (Mean Squared Percentage Error) in the longitude and latitude directions, average MSE (Mean Squared Error), and instantaneous position errors. However, the model with UTS=1.912 exhibits lower MSPE in the depth direction compared to the UTS=2.273s model. Consequently, in subsequent research endeavors, it may be beneficial to consider integrating the predictive capabilities of the UTS=1.912s model in the depth direction.

III. SEARCH AND RESCUE PATH PLANNING MODEL

A. Model Design

When the submersible loses contact with the mother ship, measures should be taken to locate the submersible as quickly and efficiently as possible. The position prediction model can give a position prediction for a period based on the last known position of the submersible sent to the mother ship before the loss of contact and the motion parameters of the previous period. Based on this model, we design a Search-and-Rescue (SAR) path planning model to help find the SAR path that maximizes the probability of SAR success and minimizes SAR time.

The mother ship first selects a starting point and then uses a position prediction model to generate a large number of position sequences, followed by a large number of path sequences from the starting point to the target submersible position. By performing Monte Carlo Simulation on these path calculation data, we can determine approximate probability distributions for the Instantaneous Position Error (IPE, E_p) and Instantaneous Velocity Error (IVE, E_v). Using the probability distributions, we

can calculate the population fitness function for each path, and then gradually reduce the population of paths through crossover, mutation and selection, and finally select the SAR path that maximizes the population fitness function. The overall process is shown in Figure 10. [10]

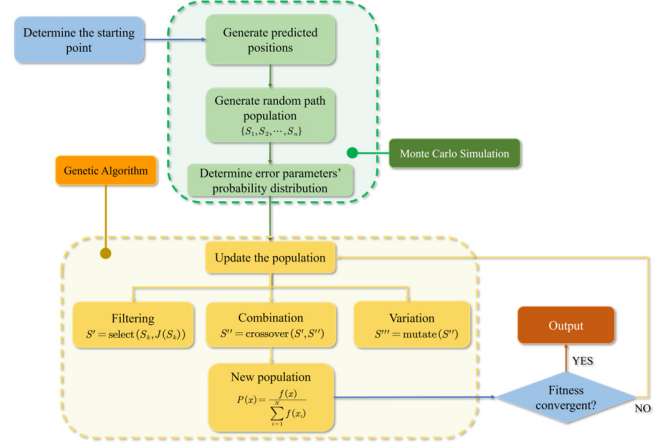


Figure 10. Our SAR Path Planning Model

B. Monte Carlo Simulation

Due to the fact that the position prediction model we have established is based on velocity calculations to provide position predictions, we determine IPE (E_p) and IVE (E_v) as error parameters, built upon the existing model. Both errors are vectors, each comprising three components in the longitude, latitude, and depth directions.

We conduct K-means clustering analysis to categorize IPE and IVE into five distinct levels. The midpoints of the four boundary lines were then chosen as the calibration values for the four sampling instances. We employ a prediction cycle of 30 minutes, equivalent to 1800 seconds, to conduct two sets of samplings on the error parameters. The first set of samplings involved sampling of IPE under different IVE conditions, while the second set involved sampling of IVE under different IPE conditions. A data point is defined as a 'Significantly Likely Point' if the data points within a radius equal to or less than 5% of that value constitute more than 5% of the total samples for the current prediction times. The 'Significantly Likely Points' and their averages from the two sets of samplings are illustrated in Figure 11 and Figure 12.

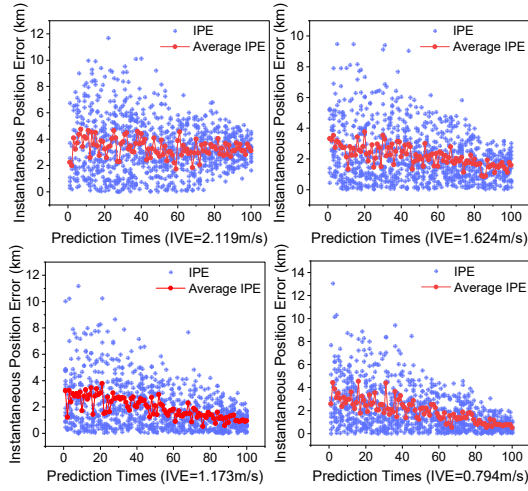


Figure 11. Sampling Distribution of IPE under Different IVE Conditions

Through graphical analysis, we observed that with an increasing number of prediction times, the means of IPE and IVE tend to stabilize around certain fixed values. According to the Central Limit Theorem, we can infer that the distribution of the means of IPE and IVE approximately follows a normal distribution. By statistical analysis, we calculated the 95% confidence intervals for the means and variances of IPE and IVE under different conditions, as presented in Table 2.

Table 2. The 95% Confidence Interval for the Error Parameters Calculated from the Sampled Data

Error Parameter with Condition	The 95% Confidence Interval for Mean	The 95% Confidence Interval for Standard Deviation
IPE (IVE=2.119)	(3.03, 3.19)	(2.603, 3.145)
IPE (IVE=1.624)	(1.25, 1.43)	(1.857, 2.341)
IPE (IVE=1.173)	(0.71, 0.92)	(1.326, 1.693)
IPE (IVE=0.793)	(0.32, 0.51)	(1.101, 1.252)
IVE (IPE=4.926)	(1.75, 1.93)	(1.421, 1.732)
IVE (IPE=3.865)	(1.50, 1.68)	(1.213, 1.472)
IVE (IPE=3.193)	(0.83, 1.04)	(1.248, 1.369)
IVE (IPE=2.268)	(0.51, 0.71)	(0.810, 1.042)

The 95% confidence intervals for the mean of IPE narrow progressively under different IVE conditions. This suggests that as IVE decreases, the average IPE becomes more stable, indicating improved prediction accuracy. For standard deviation, a similar trend is observed: as IVE decreases, the variability in IPE reduces.

As IPE increases, the 95% confidence intervals for the mean of IVE also widen, indicating that an increase in IPE leads to increased uncertainty in velocity predictions. The 95% confidence intervals for the standard deviation of IVE also widen with increasing IPE, further suggesting that the variability of prediction errors increases with higher IPE.

C. Genetic Algorithm

We first set a starting point for the SAR ship and consider each set of longitude and latitude coordinates for a search and

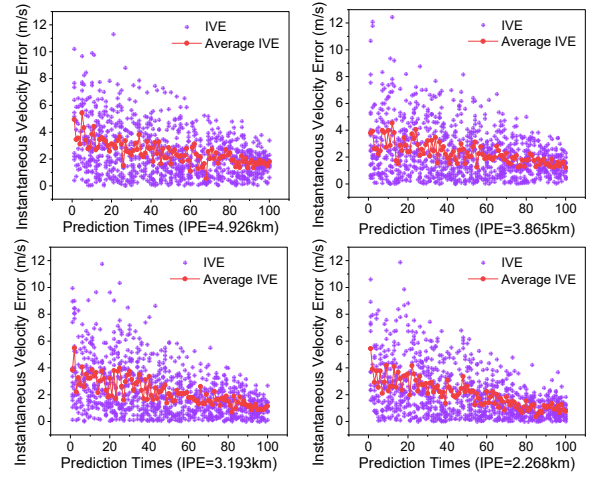


Figure 12. Sampling Distribution of IVE under Different IPE Conditions

rescue path as a “chromosome”. Based on the results of Monte Carlo Simulations and the predetermined starting point, we generate a series of weighted path sets. Here, the weights represent the total probability distribution for each path. Our objective is to maximize the probability of successful SAR. And simultaneously, we aim to maximize the probability of the path’s time being less than the time threshold, denoted as T . Therefore, we define the fitness function for the population as the product of the probabilities of IPE being less than the threshold E_p and IVE being less than the threshold E_v , added by the ratio of paths with a time less than the threshold T to the total number of paths, as expressed in Equation 7. We employ a range of crossover rates and mutation rates, conducting extensive simulations. Through these simulations, we observe that the population fitness function achieved relatively high values when the Ratio of Crossover rate to Mutation rate (RCM) is maintained at the values of 0.72, 1.067, and 1.304. In each crossover and mutation iteration, we randomly select one value from these three (0.72, 1.067, 1.304) for computation. After the first iteration, the best SAR route with the maximum value of the population fitness function is illustrated in Figure 13.

$$\text{Fitness}(S) = P(\text{IPE}(S) < E_p) \cdot P(\text{IVE}(S) < E_v) + \frac{\text{Num}(t < T)}{\text{Num}(\text{Paths})} \quad (7)$$

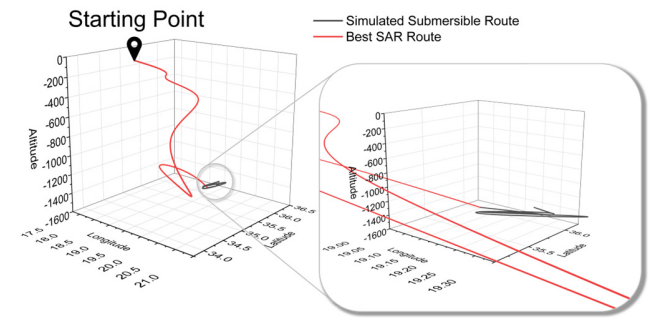


Figure 13. Result of the first iteration's predicted best path

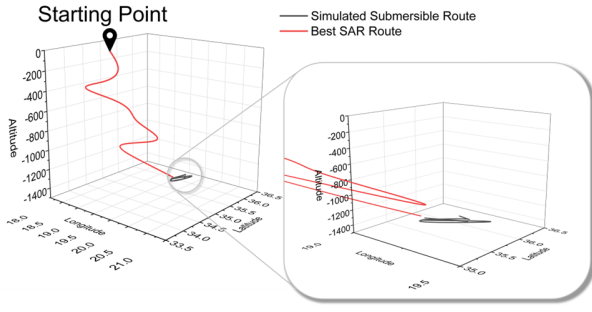


Figure 14. Result of the 1892nd iteration's predicted best path

We perform genetic iterations using Python and its DEAP library. In single selection, crossover selection, and mutation selection, we employ the tournament selection method, characterized by simpler operational principles and better maintenance of diversity within the 'population'. We set the stopping criterion for the model's iteration to be when the RMSEs for the position predictions of the top three paths are all below 10%. In this test, the model met the criterion after 1892 iterations, and the best SAR path result following this iteration is depicted in Figure 14.

D. Data Analysis

As can be seen from the results in Figure 13 and 14, after a large number of iterations, there is a significant reduction in the length of the paths planned by the model, i.e., the time used for the paths is significantly reduced. At the same time, the paths are also closer to the movement area of the submersible, thus increasing the probability of successful SAR.

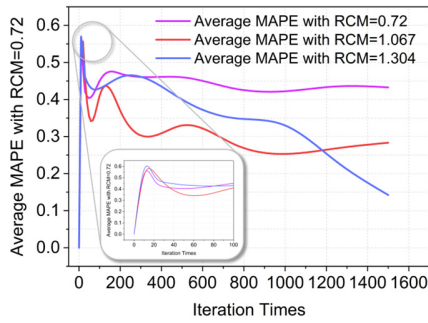


Figure 15. The Variation of Average MAPE with Iteration Times with Different RCMs

During the iteration process, the variation of MAPE with iteration count under different RCM conditions is illustrated in Figure 15. The changes in relevant mutation and crossover indicators with iteration count are depicted in Figure 16. Analyzing the data reveals that the overall performance of RCM=1.304 surpasses the other two values. Errors for RCM=0.72 and RCM=1.067 start to exhibit convergence before reaching 1000 iterations, whereas only RCM=1.304 continues to decline to a lower level even beyond 1500 iterations. The pattern with RCM=1.304 exhibits higher accuracy. Furthermore, due to our algorithm of randomly sampling values for each crossover or mutation, we introduce greater diversity into the decision-making population. We observe that crossover rates and

mutation rates generally do not exceed 50%, reflecting to some extent the stability of this path selection scheme.

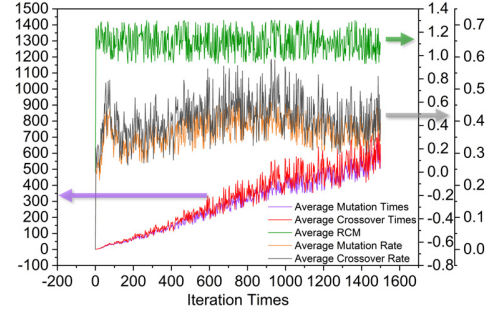


Figure 16. The Variation of Relevant Mutation and Crossover Indicators with Iteration Times

E. Adaptability Analysis

To comprehensively evaluate the performance of the path planning model, we design two tests to evaluate the model's adaptability to various environments.

In the first test, we select the Ratio of Crossover rate to Mutation rate (RCM) and the sensitivity of the fitness function (f) as the main parameters for analysis. The Mean Absolute Percentage Error (MAPE) and the number of iterations are chosen as the evaluation criteria. We set the range of the RCM from 0.7 to 1.3. Four available population fitness functions in genetic algorithms are denoted as:

$$f_1(S) = -(\mu_{IPE}(S) + \mu_{IVE}(S)) \quad (8)$$

$$f_2(S) = -(\alpha\mu_{IPE}(S) + \beta\sigma_{IPE}(S) + \gamma\mu_{IVE}(S) + \delta\sigma_{IVE}(S)) \quad (9)$$

$$f_3(S) = P(IPE(S) < \mathbf{E}_p) \cdot P(IVE(S) < \mathbf{E}_v) + \frac{\text{Num}(t < \mathbf{T})}{\text{Num}(\text{Paths})} \quad (10)$$

$$f_4(S) = -(\mu_{IPE}(S) + k_1\sigma_{IPE}^2(S) + \mu_{IVE}(S) + k_2\sigma_{IVE}^2(S)) \quad (11)$$

In section D, the function we have employed is f_3 . We separately plot heatmaps for the average MAPE and the average iteration times under different conditions of A and B, as illustrated in Figure 17 and 18.

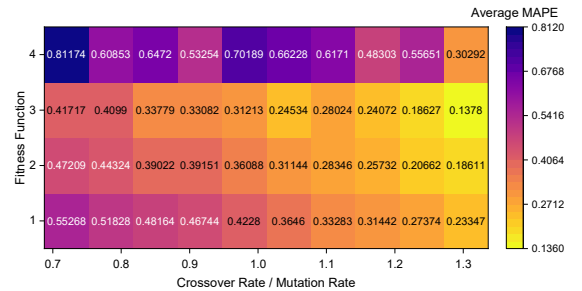


Figure 17. The Average MAPE with different f and RCM

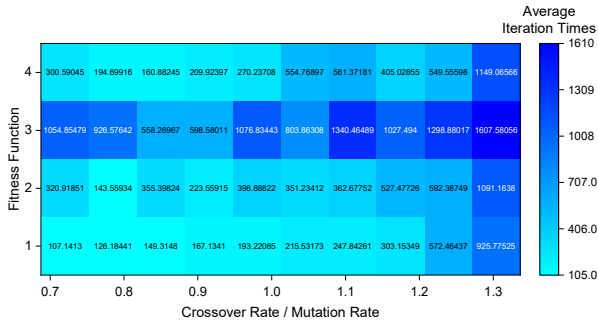


Figure 18. The Average Iteration Times with different f and RCM

The findings from Figure 17 elucidate that, holding the fitness function constant, an augmentation in the ratio of the crossover rate to the mutation rate is inversely correlated with the MAPE. Concurrently, for a static RCM, the MAPE associated with fitness function f_3 is demonstrably lower than that of f_2 , which in turn is lower than f_1 , and f_1 exhibits a lower MAPE than f_4 . Analyzing the findings from Figure 18 reveals that: holding the fitness function constant, a reduction in the RCM rate leads to a decrease in the number of iterations; moreover, at the same ratio of crossover to mutation rates, the sequence of iteration numbers is as follows: f_1 records fewer iterations than f_4 , which is followed by f_2 , and finally, f_3 requires the most iterations.

We hope that the adaptability test indicator MAPE and the number of iterations for the model are as low as possible. The trend of MAPE and the number of iterations changes in the opposite direction when the RCM and the fitness function change in the same direction. Therefore, when considering the size of the model design parameters in this marine environment, we should take into account both MAPE and the number of iterations comprehensively. A weighted method can be considered to evaluate the impact of different combination schemes on the performance of this SAR path planning model.

In the second test, we vary the current speed to simulate different sea environments in order to test the applicability of the model in different sea environments. Conditions with Change in Current Velocity (CCV) set at 2.6 m/s and 5.4 m/s are selected. We then conducted simulations using the path planning model, obtaining the average MAPE, average relative RMSE, and average iteration count, as illustrated in Figure 19 and 20.

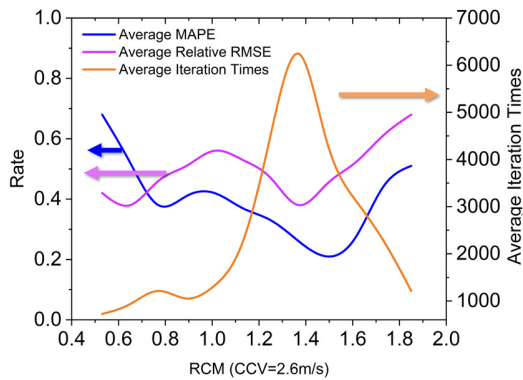


Figure 19. The average MAPE, Relatively RMSE, and Iteration Times with CCV=2.6m/s

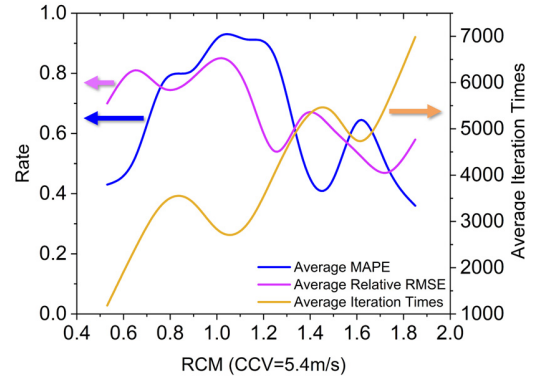


Figure 20. The average MAPE, Relatively RMSE, and Iteration Times with CCV=5.4m/s

Data analysis reveals that under different ocean current velocity change variables, the stability of the model has been significantly affected. There is a substantial increase in the average iteration count, and the distribution of errors differs significantly from the previous data. The maximum average iteration count has even risen to 7000.

In response to this situation, an adaptive learning mechanism can be introduced in different marine regions to enable the model to learn and adapt to environmental changes in real time. Techniques such as reinforcement learning can be considered, allowing the model to continuously adjust its strategy through interaction with the environment. Additionally, in future research, it is crucial to ensure that training data is sufficiently diverse, covering various environmental conditions. This includes increasing the sample size with different ocean current velocity change variables to enhance the model's accuracy and generalization capabilities.

IV. CONCLUSIONS

In this paper, we innovatively construct a submersible position prediction model based on the BiLSTM network, which is able to give the predicted position data of the submersible over a period based on the velocity data calculated by the six-degree-of-freedom kinematic model and the previous kinematic data of the submersible. We train and test the model based on current and seafloor topography data in the Ionian Sea, which shows that the model is able to achieve a prediction accuracy of over 80%.

Based on this model, we construct a search and rescue path planning model using Monte Carlo simulation and genetic algorithm, which can provide search and rescue path planning for the search and rescue of wrecked submersibles with a relatively short time and high probability of successful search and rescue.

We test the adaptability of the path-planning model to different parameters by varying the ratio of crossover rate to variability and the population fitness function, and we also test the adaptability of the model to different marine environments by varying the current flow rate. The results show that the

model's adaptability to different contexts changes relatively significantly with the parameters. Therefore, when applying this model, we suggest making the model fully learn the relevant data of the target waters and the submersible to minimize the errors generated by the environment.

Future research directions can focus on expanding the model's data intake to include more diverse environmental variables, such as water temperature, salinity, and pressure, which could influence submersible dynamics in unforeseen ways. Additionally, integrating real-time data streams into the model is able to enhance its predictive capabilities, allowing for dynamic adjustments to planned missions based on changing environmental conditions. Another promising avenue is the exploration of more sophisticated machine learning algorithms and the potential for hybrid models that combine the strengths of different approaches to further improve prediction accuracy and operational efficiency.

REFERENCES

- [1] Li Dejun, He Chunrong, ZHAO Qiaosheng, et al. Research on multi-degree-of-freedom motion modeling and simulation of submersible collaborative operation [J]. *Ship Mechanics*, 2020, 24 (03): 342-351. DOI:10.3969/j.issn.1007-7294.2020.03.008.
- [2] Roman G, Thomas D, Yu Cao, et al. Hydrodynamic loads on a restrained ROV under waves and current [J]. *Ocean Engineering*, 2021, 234. DOI:10.1016/j.oceaneng.2021.109279.
- [3] Xiang Xie, Yu Cui, Zhang Qiang. Robust fuzzy 3D path following for autonomous underwater vehicle subject to uncertainties [J]. *Computers and Operations Research*, 2016, 84 165-177. DOI:10.1016/j.cor.2016.09.017.
- [4] Ataei M, Yousefi-Koma A. Three-dimensional optimal path planning for waypoint guidance of an autonomous underwater vehicle. [J]. *Robotics and Autonomous Systems*, 2015, 67 23-32. DOI:10.1016/j.robot.2014.10.007.
- [5] Dejun Li, Wei Zhang, Lei Wang, et al. Research on motion simulation of submersible under ocean current interference[J]. *Ship Science And Technology*, 2023, 45(11). URL: https://www.zhangqiaokeyan.com/academic-journal-cn_ship-science-technology_thesis/02012101677516.html.
- [6] Cheng Ma, Lian Lian. Control and Simulation Technology of Underwater Vehicle [M]. Beijing: National Defense Industry Press, 2009. URL: https://xueshu.baidu.com/usercenter/paper/show?paperid=7dd4dcdbaf6a3be012773f718dad7f43&site=xueshu_se.
- [7] IHO, IOC. GEBCO data download[EB/OL]. [2024-02-23]. <https://download.gebco.net/>.
- [8] Chinese Academy of Sciences. Marine Science Big Data Center[EB/OL]. [2024-02-23]. <http://msdc.qdio.ac.cn/>.
- [9] Google. Google Earth[EB/OL]. [2024-02-03]. <https://earth.google.com/web/>.
- [10] Sun Bo, Jiang Ping, Zhou Genrong, et al. AGV path planning based on improved genetic algorithm [J]. *Computer engineering and design*, 2020, 41 (2): 7. DOI: CNKI:SUN:SJSJ.0.2020-02-038.